Supporting Information

Role of Micromagnetic States on Spin-Orbit Torque Switching Schemes

Jie Zhang[1,2*], Chirag Garg[2,3*], Timothy Phung[2§], Charles Rettner[2], Brian P. Hughes[2], See-Hun Yang[2], Yong Jiang[1], and Stuart S. P. Parkin[2,3§]

[1]School of Materials Science and Engineering, University of Science & Technology Beijing, Beijing, 100083, China

[2]IBM Almaden Research Center, San Jose, California, 95120, United States

[3]Max Planck Institute for Microstructure Physics, Halle (Saale), D06120, Germany

*These authors contributed equally to the work.

§ phungt@us.ibm.com; stuart.parkin@mpi-halle.mpg.de

1. Characterization of free layer magnetic properties

Magnetic characterization of the free layer was performed on blanket films that were identical to the films in which the three terminal devices were fabricated, but did not include the reference layer magnetic stack. The film stack that was characterized was 60 W(O) | 20 $Co_{40}Fe_{40}B_{20}$ | 0.50 $Co_{70}Fe_{30}$ | 16 MgO | 50 Ta | 50 Ru, with the thickness of each film layer in angstroms. Figs. S1a and S1b show the saturation magnetization (M_s) and effective magnetization (M_{eff}) measured using vibrating sample magnetometry (VSM) with field applied (H) in the easy axis and hard axis, respectively. The saturation magnetization obtained was 1234 emu/cm^3 and the effective magnetization was found to be 896 emu/cm^3.

The Gilbert damping was measured with the same blanket film using stripline ferromagnetic resonance. The ferromagnetic resonance spectrum is shown in Figure S1c, along with representative data, and their corresponding fits to a Lorentzian function (Figure S1d). The

resonant frequency (f) as a function of magnetic field is fitted to the Kittel formula (Figure S1e), where we obtain a M_{eff} of 932 emu/cm^3, consistent with the out of plane VSM measurements. The Gilbert damping is found by fitting the peak to peak linewidth (Δ) as a function of frequency, from which we obtain a damping value of 0.021 ± 0.001.

2. Methodology for micromagnetic simulations

Micromagnetic simulations were performed using the LLG Micromagnetics Simulator software. Two different geometries were considered for simulations of magnetization switching under spin-orbit torques (SOTs). The first geometry shown in Figure 2b and S3 has a magnetic nano-element with dimensions of 200 nm × 100 nm. The second geometry is in the form of a right angled trapezoid with height 74nm and bases that are 150 and 100 nm long. The simulations use a finite element cell size of 2 nm x 2 nm x 1nm. The only magnetic layer that is simulated is the free layer of the magnetic tunnel junction (MTJ). The material parameters used for the magnetic layer are: saturation magnetization, M_s = 1200 emu/cm^3, perpendicular anisotropy energy constant, K_u = 2.6 × 10^6 erg/cm^3 with the easy axis oriented along the z axis (for this anisotropy value, the magnetization is in-plane magnetized in the remnant state as the anisotropy is not significant enough to overcome the demagnetizing energy in the z direction). These values were obtained from magnetic measurements conducted using vibrating sample magnetometery (See S1). The exchange stiffness constant is taken to be A= 2 μerg/cm, and the Gilbert damping used was 0.02. The spin Hall angle, θ_{SHA} = -0.5, used in our simulations is based on the value obtained from W(O) layer in our present study, and the SOT is modeled as a damping like torque contribution. The Oersted field is also included in our simulations. All simulations were done at a constant current density of 1.5 × 10^8 A/cm^2. The current pulses have a rise and fall time of 5 ps.

3. Micromagnetic simulation of fast time scale switching dynamics in right trapezoid device

Micromagnetic simulations[1] were performed to understand the fast time scale switching dynamics of a right trapezoid device (in particular, a D_{xx-} device type). The spatial average of the normalized magnetization component in the x direction $< m_x >$ is plotted as a function of time in Figure S2a for various current pulses with current pulse widths ranging from 100 ps to 400 ps for current running in the $+x$ direction. The initial state of the magnetization in each simulation is oriented predominately in the x direction, as illustrated in the snapshot from the micromagnetic simulation in Figure S2c. The switching process occurs through four steps that can be identified from the time traces and is demarcated for the case of a 200 ps current pulse (Figure S2b). 1) The magnetization is first rotated from the $+x$ direction towards the $+y$ direction through the SOT. 2) After 200 ps, in which case the current is removed, due to the shape anisotropy induced by the right trapezoid shape, the magnetization acquires a small component in the reversed direction as described in the main text. 3) The magnetization reversal occurs through growth of a domain wall. 4) The magnetization relaxes to its final equilibrium state through precession abut its equilibrium state. Fast switching with pulse widths as short as 150 ps (See Figure S2a black line) can be achieved using this mechanism. We note further that the switching is "quasi-ballistic", and switching is achieved within almost one precession cycle[2,3]. The relaxation of the magnetization in step 4) however involves several precessions, but is deterministic. We note that unlike other fast time scale switching schemes using non-collinear moments, this scheme is insensitive to the width of the current pulse used when the current pulse exceeds a critical pulse width[4].

Figures S2d and S2e compares the switching dynamics for a non-switching and switching event. In the 100 ps current pulse width case, where switching does not occur, the magnetization

rotates towards the $+y$ direction due to the SOT, but does not have sufficient time to reorient to be fully orthogonal to the current direction. Consequently, the magnetization does not develop any component along the reversal direction at the end of the current pulse. The return of the magnetization towards its initial direction initiates from a domain formed on the *top right* corner of the nano-element. This edge is preferred given the lower shape anisotropy density. By contrast, for the 200 ps case, at the end of the current pulse the magnetization has rotated orthogonal to the current direction, and develops a component along the reversal direction, which is what later forms the nucleation point for the reversal domain that moves in from the *top left* corner of the nano-element.

4. Effect of lithographic defects on switching in the case of a D_{xx} device

Small lithographic defects at the edge of a nano-element are also significant enough to influence the switching dynamics in the D_{xx} device. To illustrate this, we consider three different magnetic nano-elements of dimensions 200 nm × 100 nm in the D_{xx} configuration where we apply identical current pulses as to what is used in the simulations shown in Figure 2c of the main text, which are 500 ps long current pulses with current density of 1.5×10^8 A/cm^2.. In the first case (Fig S3a-S3b), the nano-element is a perfect rectangle but in the other two cases a defect is introduced in the form of a missing voxel that is 6 nm × 6 nm in size at either the top-left (Fig S3f-S3g) or the bottom-left (Fig S3k-S3l) corner of the nano-element. Each figure (S3a-S3b, S3f-S3g, and S3k-S3l) shows the relaxed sate of the magnetization for each structure. We shall refer to these devices as device #1, #2 and #3 in the following discussion.

In the relaxed state of device #1, although the moments curl towards the edges under the influence of the demagnetizing field, the net magnetization along the y-axis, $< m_y >$ is zero.

When a current pulse is applied across the W(O) layer, the Slonczewski-like torque from the spin Hall effect will cause the magnetization to rotate temporarily towards the direction orthogonal to the easy axis. When the current pulse is removed, the magnetization relaxes towards the easy axis in the same orientation as the initial state of the nano-element, as shown in the end state of the magnetization upon the application of a positive $(+I_x)$ and negative $(-I_x)$ current pulses (Figures S3c, and S3d, respectively). This dynamics is shown in the time evolution of the spatial average of the magnetization in the nano-element $< m_x >$ upon the application of the current pulses (Figure S3e). There is no switching here because when the SOT brings the magnetization orthogonal to the easy axis, there are no additional torques present to cause magnetization rotation.

In the case of device #2 (Figure S3f-S3g), a defect is introduced at the lower left corner and the relaxed magnetization state acquires a finite m_y component in the form of edge domains in the nano-element. The relaxed state shown here is referred to as the S-state. We note that the m_y component is correlated to the state of the m_x component (that is, the S-state has two different orientations). This S-state is stabilized due to the placement of the defect which induces internal magnetostatic fields and breaks the symmetry along the y-axis. Upon application of a current pulse, the magnetization rotates towards the spin accumulation direction. However, the demagnetizing field induced from the edge geometric defect provides an additional torque to drive reversal. Hence a switching is observed upon removal of the current pulse (Figure S3h). For the opposite current pulse polarity (Figure S3i), the internal fields act in $+x$ direction, and no switching is observed. The time evolution of the magnetization during this switching process is summarized in Figure S3j). Here the "quasi-ballistic" nature of the switching process is evident as well.

The defect is placed on the opposite edge for device #3, and thus, the sense of internal magnetostatic fields is opposite. We note that the orientation of the S-state in the remnant state of the magnetization is opposite to the second case (Figure S3k and S3l). As a consequence of the position of defect, not only are the remnant states different, but the switching behavior with respect to the current polarity is reversed (Figure S3m-S3o). Thus, the position of these small lithographic defects is critical in influencing both the remnant state as well as the switching current polarity.

A remarkable feature of the D_{xx} switching process is that the switching process is characterized by a monotonic evolution of $< m_x >$ as well as a coherent rotation of moments across the entire free layer. (as evidenced by the plots of the time evolution of the magnetization (Fig S3j and Fig S3o). In contrast, the D_{xy} devices show a non-monotonic evolution in time of $< m_x >$ as well as non-coherent reversal, involving many metastable states. As a result, the switching times can be much longer for D_{xy} in comparison to D_{xx} (see Supplementary Section 4).

In addition, for the current magnitudes considered, the magnetization reaches an effective steady state value within the duration of the 500 ps pulse. This same steady state condition can also be observed when a pulse of the same current magnitude is applied to Device #2 and left on after the ramp duration but with a significantly lower ramp rate (lasting for 5 ns) (See Figures S4a and S4b for the results of a micro-magnetic simulation with such a current pulse). Thus the magnetization configuration shown in the 500 ps time stamp magnetization maps in Figures 2d and 2e of the main text, are not the result of the abrupt current pulse used.

We also note in the case that the defects are symmetrical in the device and share a common edge, switching does not occur. In this case, the remnant state magnetization corresponds to a C-state (Fig S5a-S5b). Accordingly, the edge domains point in opposite direction both in the remnant

state and upon the application of current pulse. Under the application of current pulse to the W(O) layer, the demagnetizing fields induced by the defects provide torques on the edges of the nano-element in opposite directions. Thus, there as is no net m_x component generated at the end of the current pulse and switching cannot occur (Figure S5c-S5e).

5. Micromagnetic simulation of the D_{xy} device

Micromagnetic simulations were performed on the D_{xy} device to compare its switching dynamics with the D_{xx} device. The simulations were performed on a rectangular device with dimensions of 200 nm × 100 nm, identical to the D_{xx} device considered in Figure S3a, and for current pulse lengths ranging from 200-1200 ps. The evolution of $< m_x >$ with respect to time (S6a) during the current pulse is non-monotonic. Moreover, the D_{xy} device involves many precession cycles for switching to occur, while the D_{xx} device switches within one precession cycle.

Time resolved magnetization maps from the simulations show that the magnetization reversal process under a 600 ps current pulse for the D_{xy} is complex and incoherent, involving a non-uniform magnetization state with the nucleation of many vortices (Figure S6b). In contrast, the magnetization maps as shown in Figure 2b in the D_{xx} device do not involve the excitation of high order spin wave modes, and are more coherent. Indeed it is the excitation of these modes that leads to a non-monotonic reversal process and requires longer current pulses to complete a reliable switching event. Moreover, one can observe from the plot of the time evolution of $< m_x >$ that the precession frequency is non single-valued, indicating that different regions of the magnetic nano-element precess at different frequencies.

6. Equivalent circuit model of NOT gate

Figures S7a and S7b show an equivalent circuit model of the non-volatile inverter device illustrated in Figure 4. The circuit model for the NOT gate contains two MTJ resistances labeled as D_{xx+} and D_{xx-}, and the W(O) layer labeled as a resistance $R_{W(O)}$. In the write mode (Figure S7a), V_{OUT} is connected to ground and the voltage input is applied across $R_{W(O)}$. During the read mode, V_{IN} is disconnected from the circuit, while a voltage is applied to a terminal of $D_{xx+}$and one of the terminals of $D_{xx-}$is grounded. V_{OUT} is measured at the connection between the magnetic tunnel junctions (at the spin Hall layer), which will be an equipotential. In a realistic device application, the supply voltage V_{DD} and the ground on signal on D_{xx-} can be left connected during the entire device operation since the tunnel junction resistance is much larger than the resistance of the spin Hall layer, so during the application of V_{IN} across the spin Hall layer during the write mode, most of the current will flow across the spin Hall layer.

References:

(1) Scheinfein, M. R. LLG Micromagnetics Simulator. *LLG Micromagnetics Simulator*.

(2) Schumacher, H. W.; Ravelosona, D.; Cayssol, F.; Wunderlich, J.; Chappert, C.; Mathet, V.; Thiaville, A.; Jamet, J. P.; Ferre, J.; Haug, R. J. Control of the Magnetic Domain Wall Propagation in Pt/Co/Pt Ultra Thin Films Using Direct Mechanical AFM Lithography. *J. Magn. Magn. Mater.* **2002**, *240* (1–3), 53–56.

(3) Back, C. H. Minimum Field Strength in Precessional Magnetization Reversal. *Science (80).* **1999**, *285* (5429), 864–867.

(4) Kent, A. D.; Özyilmaz, B.; Del Barco, E. Spin-Transfer-Induced Precessional Magnetization Reversal. *Appl. Phys. Lett.* **2004**, *84* (19), 3897–3899.

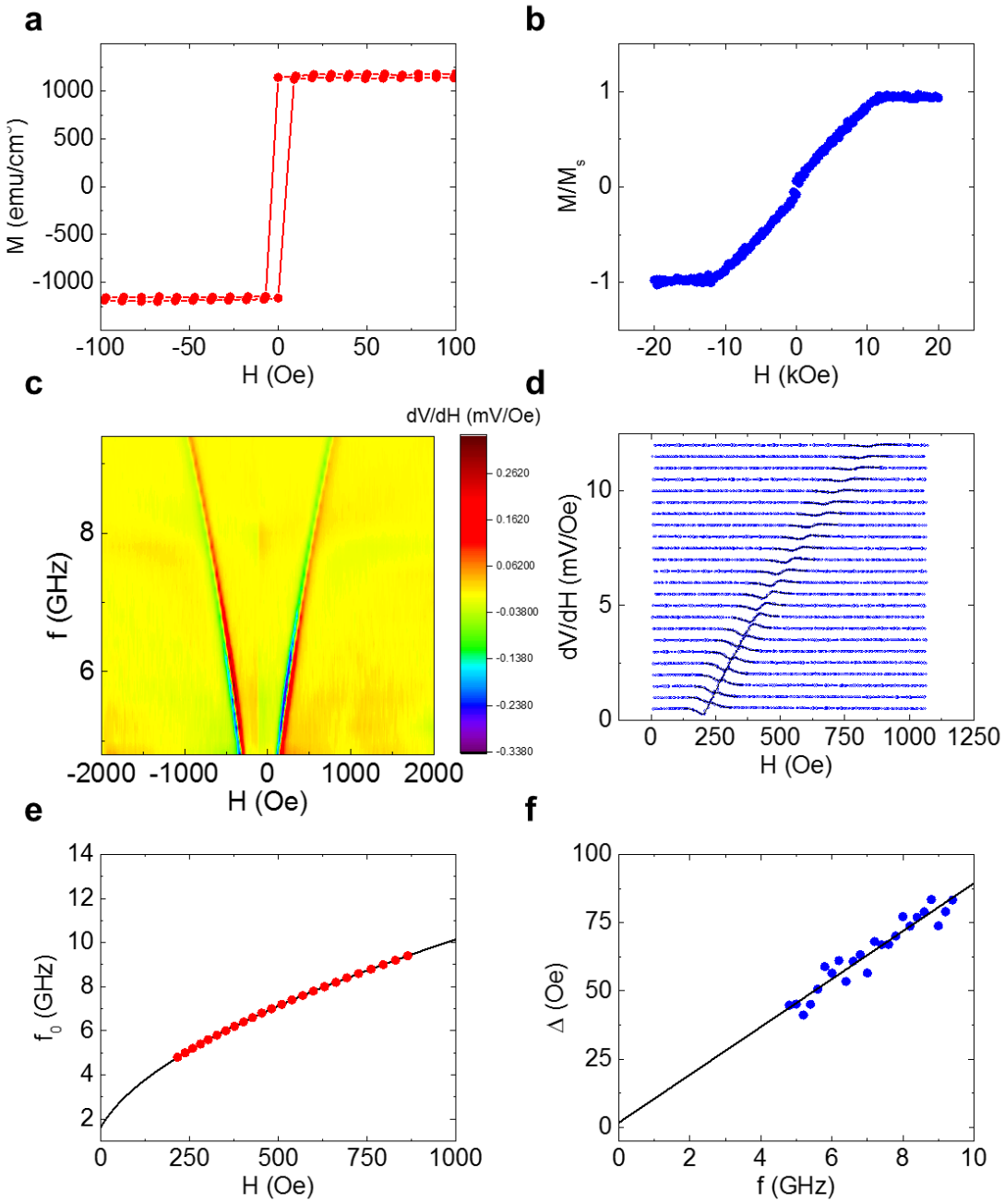

Figure S1. (a) VSM measurement of magnetic moment as a function of magnetic field measured with magnetic field applied in-plane to determine saturation magnetization. (b) Determination of effective magnetization by VSM measurement of magnetic moment vs. applied magnetic field applied out of plane. (c) FMR spectra measured using stripline ferromagnetic resonance. (d) Representative FMR data and fits to determine the resonant frequency and linewidth. (e) Resonant frequency as a function of field (red symbols), and Kittel formula fit (black line). (f) Peak-to-peak linewidth as a function of RF frequency applied to the stripline (blue symbols) along with linear fit (black line) to determine the Gilbert damping parameter.

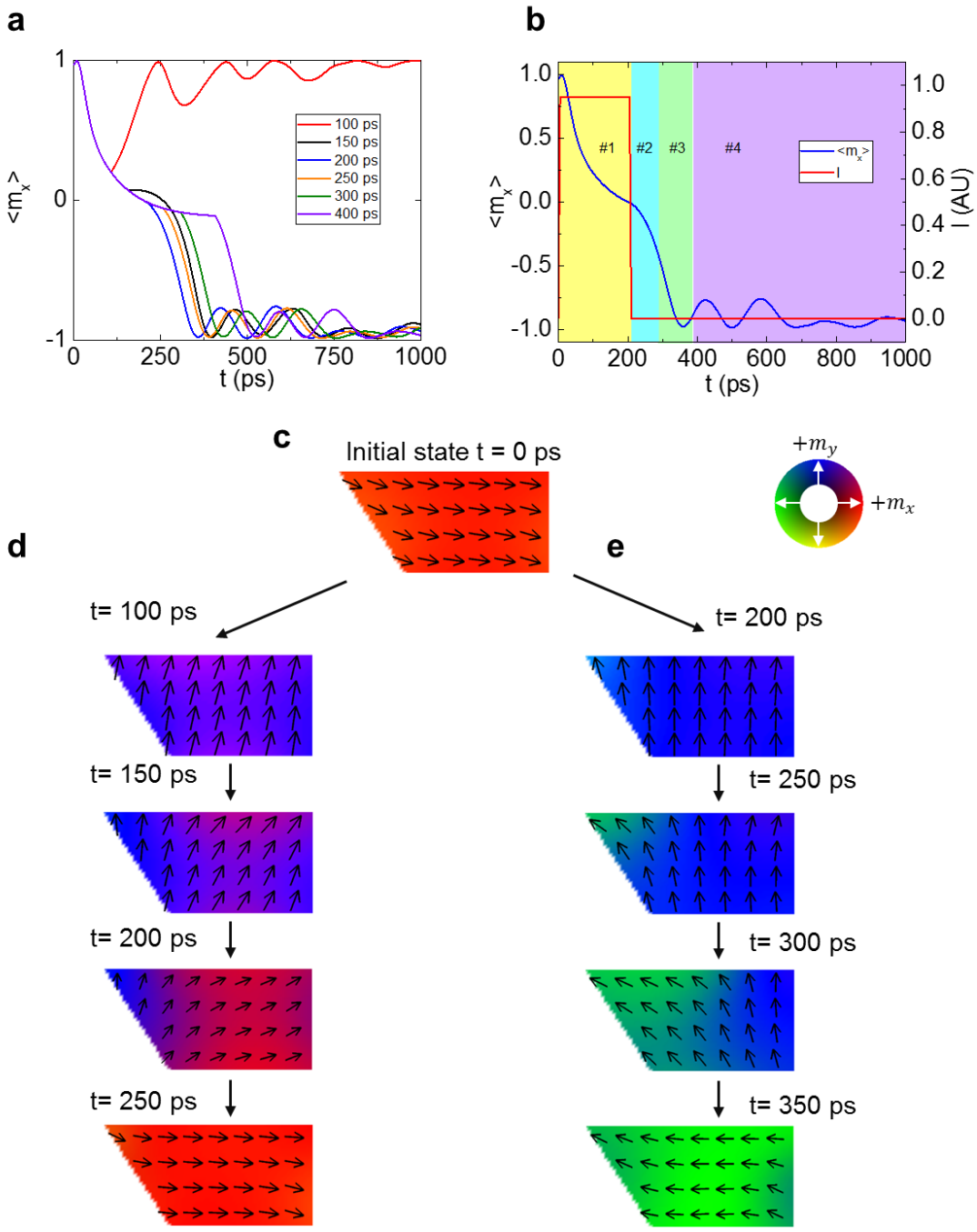

Figure S2. (a) Time evolution of $< m_x >$ for various current pulses for a D_{xx-} device. (b) Current pulse and magnetization vs. time for the 200 ps case, with 4 step magnetization reversal process outlined. (c) Magnetization configuration of initial state for a right trapezoid device D_{xx-} type as calculated by micromagnetic simulations. (d) Magnetization maps showing time evolution of magnetization for a *non-switching* event with a current pulse width of 100 ps. (e) Magnetization maps showing time evolution of magnetization for a *switching* event with a current pulse width of 200 ps.

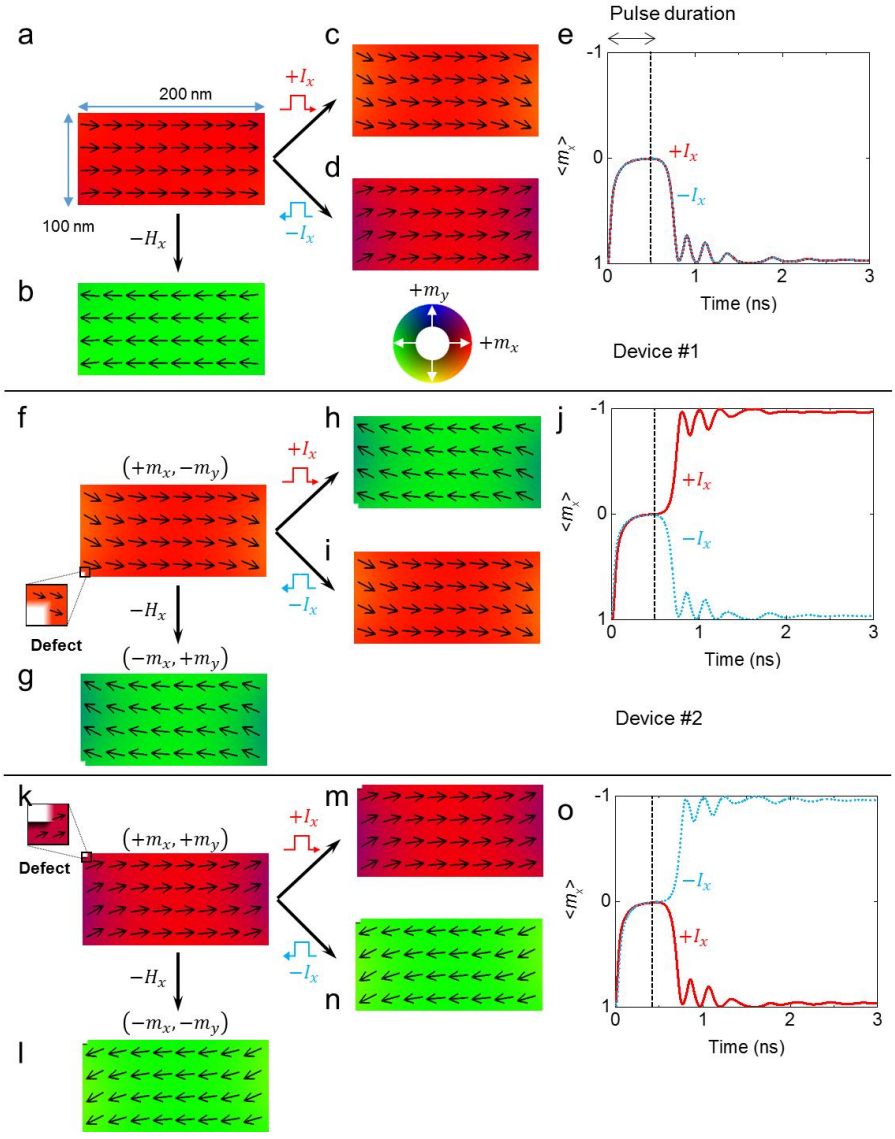

Figure S3. (a,b) Magnetization configuration of remnant state for a rectangular D_{xx} device with no defects for the (a) $+x$ and (b) $-x$ magnetization directions. (c,d) Final state magnetization map after application of 500 ps current pulse for (c) positive and (d) negative current polarity current pulse. (e) Time evolution of average magnetization $< m_x >$ under positive (red-line) and negative (blue-dotted line) current pulses. (f,g) Magnetization configuration of remnant state for a rectangular D_{xx} device with a defect on the bottom left edge for the (f) +x and (g) -x magnetization directions. (h, i) Final state magnetization map after application of 500 ps current pulse for (h) positive and i negative current polarity current pulse. (j) Time evolution of average magnetization $< m_x >$ under positive (red-line) and negative (blue-dotted line) current pulses. (k,l) Magnetization configuration of remnant state for a rectangular D_{xx} device with a defect on the top left edge for the (k) $+x$ and (l) $-x$ magnetization directions. (m, n) Final state magnetization map after application of 500 ps current pulse for (m) positive and (n) negative current polarity current pulse. (o) Time evolution of average magnetization $< m_x >$ under positive (red-line) and negative (blue-dotted line) current pulses.

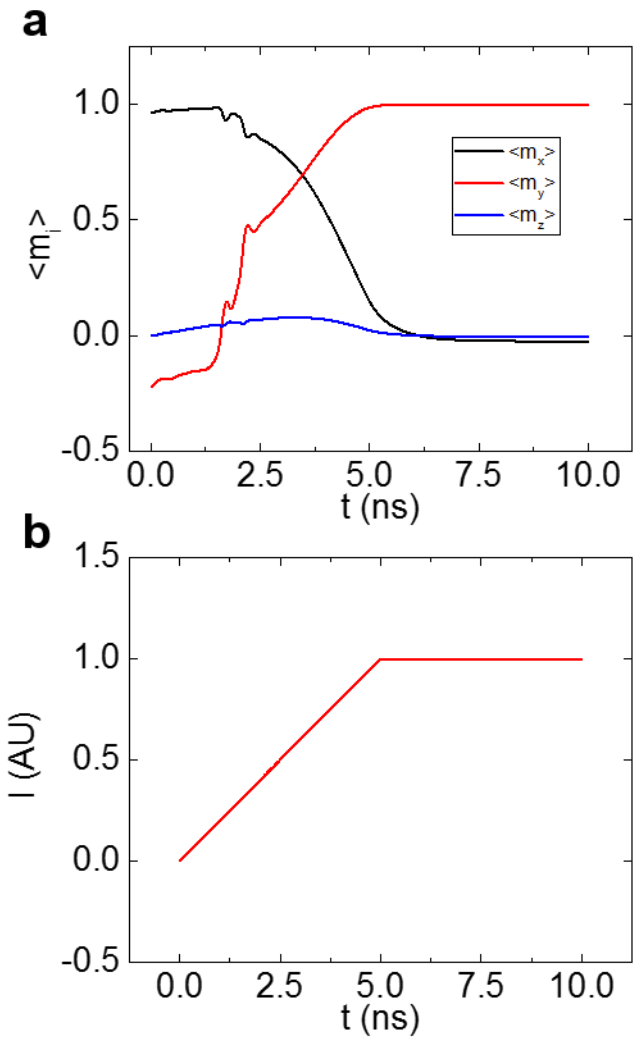

Figure S4. (a) Time evolution of $< m_x >$, $< m_x >$, and $< m_z >$ from micromagnetic simulations for a current pulse with a 5 ns ramp time. (b) Current pulse used in micromagnetic simulations

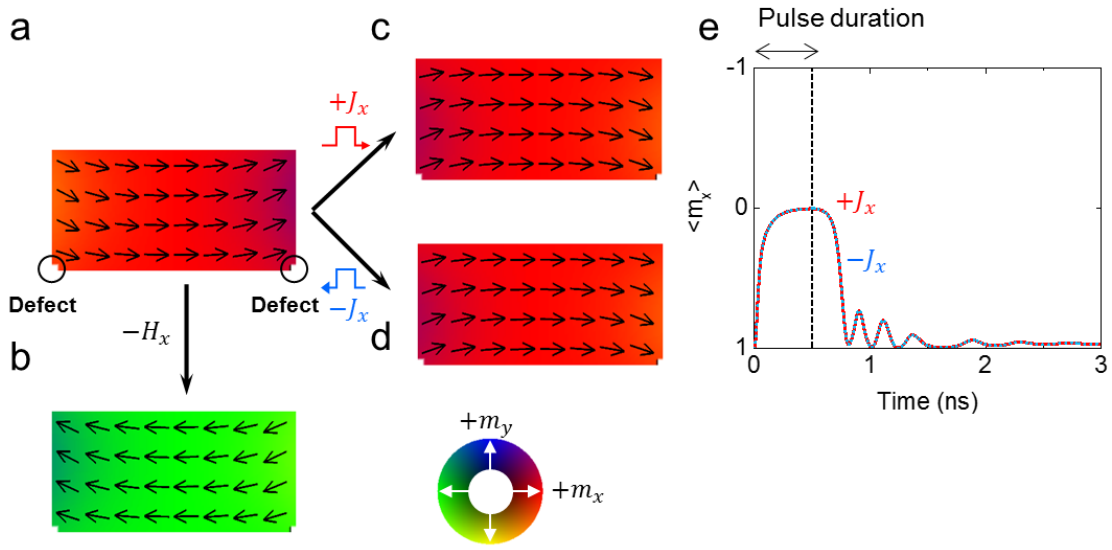

Figure S5. (a,b) Magnetization configuration of remnant state for a rectangular D_{xx} device with symmetrical defects for the (a) $+x$ and (b) $-x$ magnetization directions showing stabilization of the C-state. (c,d) Final state magnetization map after application of 500 ps current pulse for (c) positive and (d) negative current polarity current pulse. (e) Time development of average magnetization $< m_x >$ under positive (red-line) and negative (blue-dotted line) current pulses.

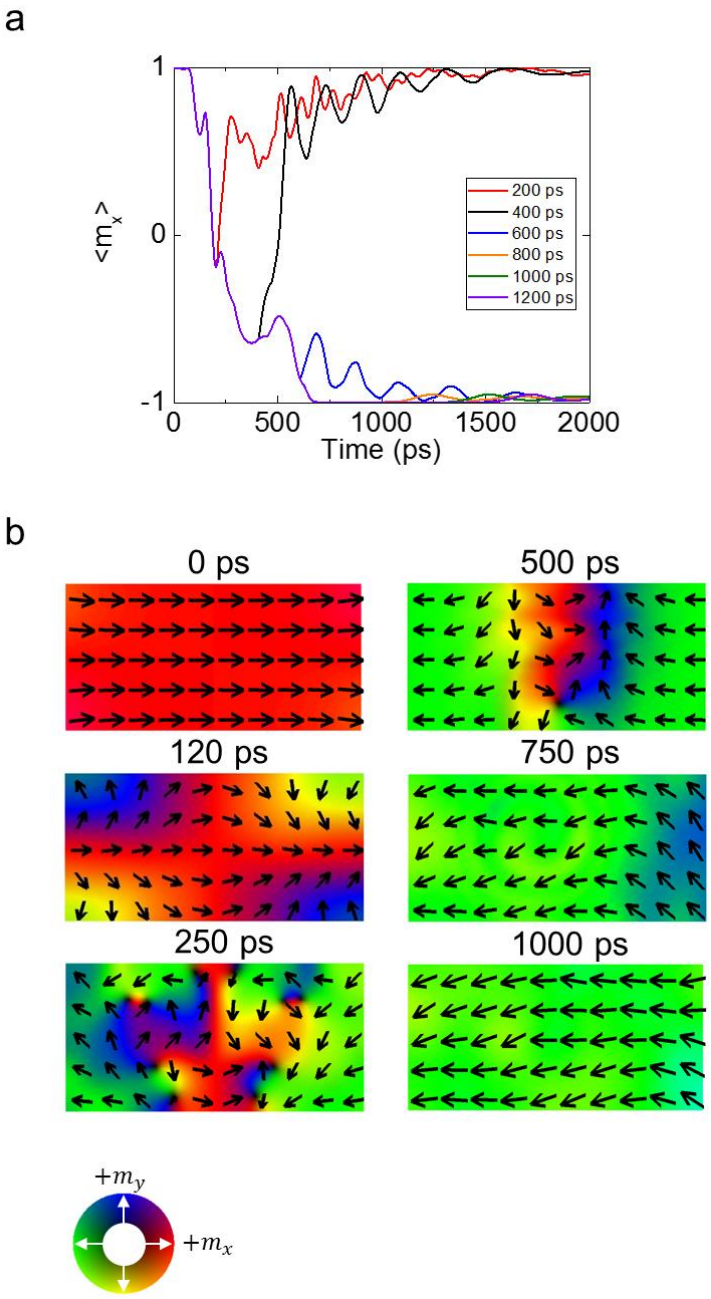

Figure S6. (a) Time progression of $< m_x >$ for various current pulses for a D_{xy} device. (b) Magnetization maps showing time evolution of magnetization for a switching event with a current pulse of 600 ps.

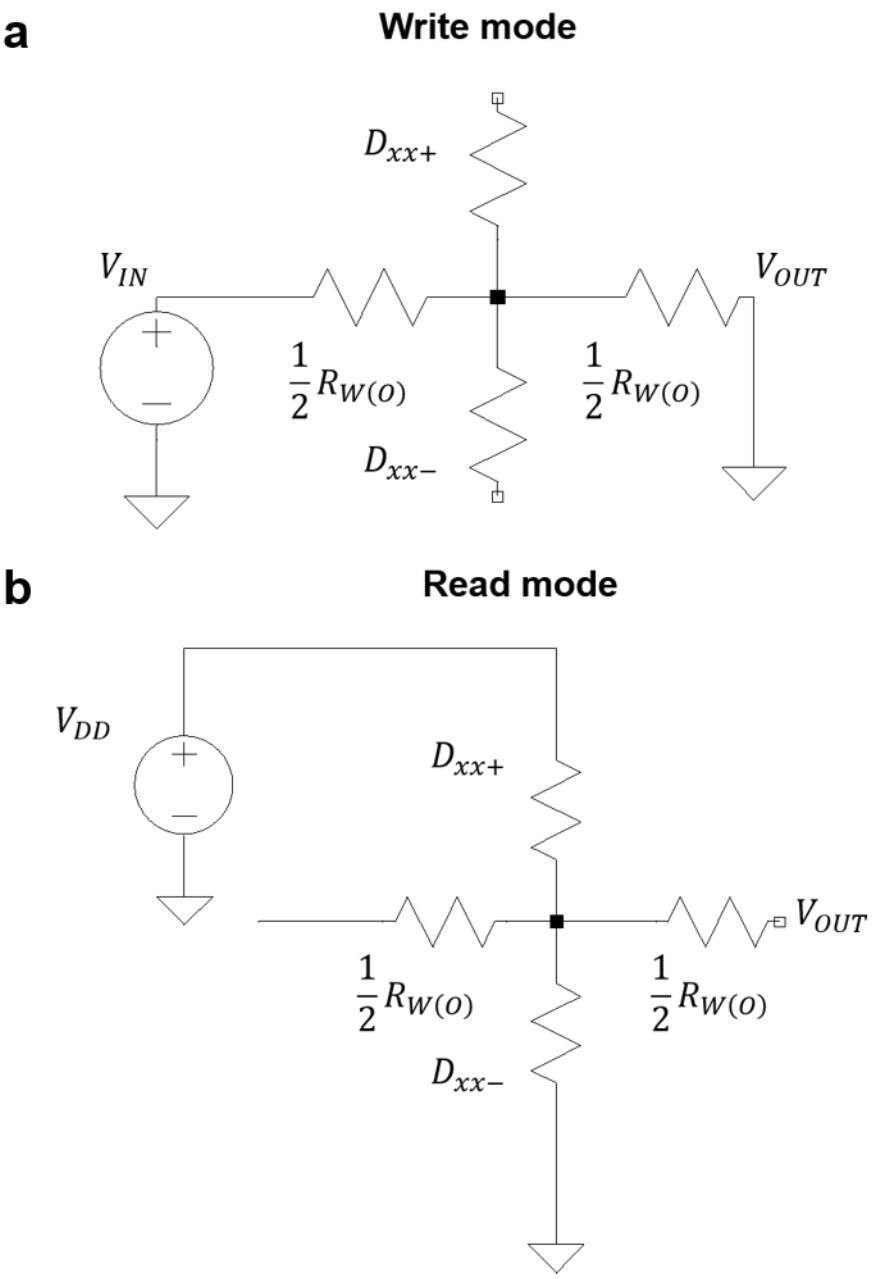

Figure S7. (a, b) Equivalent circuit diagram of the non-volatile (NOT gate) inverter circuits in the (a) write and (b) read mode.